RAL-TR-2005-010

A MONTE-CARLO MODEL OF SPATIAL RESOLUTION IN X-RAY IMAGING GAS COUNTERS – A STUDY OF THE BASIC PHYSICAL LIMITATIONS

J.E. Bateman

Rutherford Appleton Laboratory, Chilton, Didcot, Oxon, OX11 0QX, UK

1 August 2005

Abstract

X-ray imaging counters which utilise some form of gas-avalanche technology (parallel gaps, wires or point anodes) have a history stretching back at least three decades and the inexorable advance of micro-electronic technology continues to provide more variations on the basic theme (e.g. gas microstrips, micro-dots, GEMs, Compteur a Trous, etc.). The spatial resolution obtainable from any particular device is a complex convolution of the various processes which intervene between the absorption of the x-ray in the gas and the final evaluation of a particular statistic in the electronic readout (or the attached computer) which represents the position of this interaction. The quantised and statistical nature of the processes involved make Monte-Carlo modelling particularly appropriate and the great computing power of modern personal computers (PCs) makes the task viable. This approach is seen as a partial replacement for the traditional role of the prototype in the design process for detectors. In this report the code developed to model the performance of practical imaging detectors is modified to permit an exploration of the physical limitations on imaging with gas mixtures based on argon and xenon in the x-ray energy range 1keV to 20keV.

1. Introduction

The imaging gas avalanche counter is a long-established option for x-ray imaging in the energy range of a few to around 20keV for a wide range of applications in bio-medical, materials science and astronomy. At Rutherford Appleton Laboratory (RAL) recent efforts have been concentrated on the development of the gas microstrip detector (GMSD) [1] as a high rate, high spatial resolution detector for x-ray scattering experiments on Synchrotron Radiation Sources (SRS) and neutron scattering experiments on Spallation Neutron Sources (SNS). This work is based on the extensive work by many groups (world-wide) to make the GMSD a possible technology for application in the extreme conditions of particle tracking in Particle Physics [2]. Examples of this are seen in references [3,4] and on-going developments of these technologies are well advanced for application on the new RAL SRS machine (DIAMOND) currently under construction and the existing SNS machine (ISIS). In the course of these developments it was found that the inexorably rising costs of prototype production were being matched by the equally inexorable rise in desk-top computing power. This led to a rising emphasis of computer modelling in the design process to short-circuit some of the design stages traditionally carried out by prototyping [5].

The spatial resolution obtainable from an x-ray gas avalanche counter results from a convolution of the basic physical conversion and amplification processes with the precise treatment which the readout applies to determine a spatial resolution parameter. The first stage of this process is essentially quantised and stochastic in nature and so eminently suitable for simulation in a Monte-Carlo model which applies with minor adaptation to any form of gas amplification (parallel gap, line or point anodes). Simulation of the readout varies in complexity but is, in general, easily approximated. In the context of the development of the GMSD a key interest is in the interaction of the conversion "resolution" with the sampling limitations of the detector strip widths. As a comprehensive model of the detection process evolved it became clear that (with care) it could be applied to all forms of electronic readout and could simply be adapted to predict the intrinsic spatial resolution limits set by the conversion/avalanche processes. This is the work presented in this report.

2. Spatial Resolution of X-rays in Gas Avalanche Detectors

Practical exploitation of x-ray gas imaging counters is conventionally centred on the copper K_α line energy at 8keV although rare applications may extend from a few up to ≈20keV. In this range the noble gases argon and xenon are universally used as the main x-ray converter combined with a fraction of quencher gas – typically 10% to 20% of a suitable hydrocarbon. The quencher has essentially negligible x-ray stopping power but is essential for stabilising the avalanche process and cooling the secondary electrons in their drift to the amplifying anode.

The primary interaction of an x-ray with a (noble) gas atom is usually to eject a photo-electron from an accessible atomic shell (K, L, M in the case of argon and L, M in the case of xenon in our energy range) leaving behind a primary hole which is filled either by a fluorescent process (in which a lower energy x-ray is emitted) or by an

auger electron (again of lower energy). These in turn leave a hole in a lower shell which is filled from even lower energy shells with a cascade of very low energy electrons which dissipate the residual energy of the event. The photo-electrons (PE) and auger electrons (AE) ionise the counter gas locally to the x-ray interaction and the secondary electrons then drift down under the influence of a suitable drift field towards the high electric field of the amplifying anodes. There in the high electric field each secondary electron generates its own avalanche (usually aggregated by the amplifier time constants used in the readout system) to generate a plasma of electrons and ions which is separated by the electric field to generate the dipole signal which is detected by the readout amplifiers.

In our x-ray energy range the dominant fluorescent yields in both gases are ≈10%. The argon K fluorescence (≈3keV) has an attenuation length of 3.18cm in pure argon and generally escapes from a detector of typical centimetre dimensions without converting. The xenon L fluorescence (≈4keV) has an attenuation length of 0.45cm and generally will convert in the counter volume. However (as will be demonstrated), this dimension is so great compared with the spatial resolution generated by the PE/AE signal that it appears as a baseline background of pulses. In other words the useful spatial resolution of the gas detector originates in the PE/AE energy deposits only.

The readout amplifiers can be attached either to the anode electrodes or (for example) to mutually orthogonal strips on cathode planes which detect the dipole induction signal released as the positive ion cloud leaves the anode region. There are various readout methods which develop a spatial position parameter from these pulses – resistive divide [6], coupling cathode induction pulses to artificial delay lines [7], using differential induction pulse pick-up [8], putting analogue to digital converters (ADC) on either anode or cathode strips and evaluating the centroid of the distribution [9], or finally, one can with fine amplifying structures, rely on the spatial position of the structure and simply count the pulses in each channel [10].

Each readout method has its pro's and con's and tends to suit some counter geometries better than others so that there is no universal preferred solution. However, the spatial resolution performance of all detectors is ultimately limited by the processes taking place in the counter gas even in the presence of a "noiseless" readout. The spatially dispersive processes are:

2.1 PE/AE Electron Range: The range of fast electrons in any material (R_e) is a rapid function of their kinetic energy E_e ($R_e \approx E_e^{1.5}$) and, for example, in argon at NTP this range reaches millimeter dimensions at $E_e \approx 10$keV. The augers are isotropic in distribution while the photo-electric effect has a $\sin^2\theta$ differential cross-section (relative to the incident x-ray direction); however, the intense multiple scattering in high Z gases such as argon and xenon make photo-electron emission effectively isotropic. (See reference [11] for a discussion.) The AE energies are fixed and mostly just a few keV in both argon and xenon; however the PE energy rises linearly as the x-ray energy (E_x) rises above the dominant absorption edge. Thus for an ensemble of x-ray events (from a point beam) the secondary electrons are spread over a sphere of radius R_{PE}, the PE range. As will appear, this effect comes to dominate the

spatial resolution in the top half of our energy range.

2.2 Secondary Electron Statistics: The average number of secondary electrons (SE) generated by the primary photo and auger electrons associated with any given x-ray event is $N_{SE} = \Sigma(E_{PE} + E_{AE})/W$ where W is the mean energy per ion pair of the gas mixture. Fortunately, this is a relatively insensitive parameter and can be set at $W = 27eV$ for a wide range of argon and xenon mixtures to an acceptable approximation [12]. The variance on this number is given by $\sigma_{SE}^2 = F_A N_{SE}$ where F_A is the Fano Factor and is ≈ 0.17 for argon mixtures [12]. Thus a 5.9keV ($Mn K_\alpha$) x-ray will (on average) produce 219 secondary electrons with a full width at half maximum (FWHM) of 6.6%. N_{SE} feeds into any calculation performed by the readout in order to evaluate (for example) the centroid of the SE distribution in the presence of a fixed electronic noise; so one expects to find a component of the spatial resolution which varies as $1/E_x$.

2.3 Electron Drift Diffusion: Since the gas has a relatively low stopping power, the secondary electrons are generated over a significant distance from the gain structures (typically tens of millimeters) and are transported down onto the gain anodes by an electric drift field E_D. Diffusion is a thermal process and a given electron will move away from its point of origin in a random walk reaching a typical distance $x = \sqrt{(2Dt)}$ after a time t (D is the diffusion constant). Increasing the drift field reduces the drift time (t) and therefore the diffusion error (x) but eventually the energy pumped into the electrons heats them up so that there is an optimum value of E_D, above which the diffusion spreading increases again. The diffusion spread is a normal distribution and it is quantified as the standard deviation (SD) induced by 1cm of drift at any given value of E_D. This is notated usually as $\sigma_0(E_D)$ and is quoted in $mm/\sqrt{cm}$. The SD of a point-like cloud of electrons drifted over a distance d cm is thus $\sigma_x = \sigma_0\sqrt{d}$. In argon and xenon mixtures with alkane quenchers a typical optimum value of $0.2 mm/\sqrt{cm}$ is obtained with $E_D \approx 400 V/cm$. A review of relevant experimental data is to be found in reference [13]. The consequence of this process is that after a planar drift of 1cm at standard temperature and pressure (STP) the footprint of a point-like cloud of electrons on the amplifying structure is a normal distribution with a FWHM of $\approx 0.5 mm$. This footprint is independent of the x-ray energy; however, if (for example) a centroiding readout algorithm is used, the statistical accuracy with which the centre of the distribution can be measured is proportional to $1/\sqrt{N_{SE}}$ i.e. $1/\sqrt{E_x}$.

2.4 Electron Avalanche Gain: The initial SE charge signal is amplified to a useful level by electron-mediated collision ionisation in the high electric field near the gain structure, be it wire, point or small parallel gap. This is an inherently (stochastically) noisy process and a single electron multiplies to become a sample of a wide quasi-negative exponential distribution known as the single electron distribution (SED). The integral pulse height (PH) for the x-ray event is just the sum of a random ensemble N_{SE} of samples multiplied by the mean gas gain. The relative variance of the pulse height distribution is $\sigma_{PH}^2 = (F_A + \sigma_r^2)/N_{SE}$ where σ_r is the relative SD of the SED. The avalanche process is a highly stochastic process resulting in the finding that the PH

resolution (the relative FWHM of the PH distribution of an ensemble of x-ray events) is remarkably uniform over a wide range of anode structures, gas gain and gas mixture. The typical value observed for Mn K_α x-rays (5.9keV) is FWHM = 15%. (See reference [12] for a review of these matters.) Using this figure one derives (from the formula for $\sigma_{PH}{}^2$ given above) a value of σ_r = 0.844 for the relative variance of the SED.

2.5 Electronic Noise: With the successful production of an amplified charge pulse, the quality of the spatial information achievable is further determined by the geometry of the readout electrodes, the white noise in the front-end preamplifiers and any signal coupling losses and intrinsic noise associated with the readout technology chosen. For a given detector design these effects can generally be subsumed in a single noise value. This will have a useful relative significance but will not be easily compared between different readout methods.

3. The Monte-Carlo Model

Clearly, the code of the Monte-Carlo model must simulate the processes enumerated in Section 2 in order to represent the performance of an imaging detector and also simulate the parameterisation made by the different types of readout which may be of interest. The viability of the procedure depends on maintaining the computing time required within acceptable limits while retaining all the significant physical features of the situation. Since the methodology is based on following the fate of every SE produced in an event, (50 000*20/0.027 = 37 x 10^6 electrons are generated for a typical ensemble or spectrum of 50 000 x-ray events of 20keV) it is important to apply all valid approximations and simplifications to avoid unnecessary computing load. Those used will be explicitly listed below in the appropriate context.

The principal physical processes which must be modelled are as follows:

3.1 X-Ray absorption: The probability of absorption of an x-ray of a given energy is calculated according to the cross-section (measured in units of cm^2/g) derived from polynomial fits to the ln-ln plots of the data presented in reference [14] for argon and xenon. (Absorption on the quencher present is ignored as being negligible.) The events are partitioned pro rata between the accessible atomic shells but interactions on shells below the M shell are ignored as negligible in our energy range. As noted above, the useful spatial resolution is due to the cascade of primary electrons released from an atom by the energy of the absorbed x-ray. This cascade is truncated at the M shell and the energy normalisation maintained by assigning the mean binding energy of the M shell to a single residual electron. The worst case occurs in xenon where the residual energy is ≈1keV. However, the range of an electron of this energy in general makes a negligible contribution to the spatial resolution. Every primary electron emitted is assigned a random orientation in space.

3.2 Primary electron range: The energy of each primary electron is dissipated in ionising (and exciting) the gas in a random walk. Modelling the spatial resolution accurately depends on having a good model for this process.

Previous Monte-Carlo studies [11] have shown that in high Z gases such as argon and xenon the range is heavily affected by elastic scattering and a simple model of isotropic emission with a normal distribution about a radial range fits the available experimental data very well. The stopping power of any quencher present is ignored and the parameters for argon and xenon derived from the model of reference [11] are used. Modelling the random walk of every primary electron in detail would take us into super-computer requirements so a simple model for the ionisation density as a function of the range is required. The intense elastic scattering comes to our aid in this problem and makes a simple uniform generation of secondaries appear to give very plausible results for the spatial resolution.

3.3 Electron drift and diffusion: As noted above, the precise value of the diffusion constant σ_0 depends on the gas mixture and the drift electric field. However for simulation purposes, σ_0 wraps up all these effects in a single parameter. Thus, while for absorption and electron range we ignore the quencher, in the case of σ_0 the value for a typical hydrocarbon proportion (10% - 20%) is assumed since the quencher is dominant in cooling the drifting electrons.

3.4 Avalanche gas gain: The stochastic noise induced in the charge signal by the gas avalanche process is simulated by selecting a sample from a suitable single electron distribution (SED) for every secondary electron in each event. As discussed above, a relative SD of the SED of 0.844 is required to produce the canonical PH resolution of 15% FWHM for Mn K x-rays (5.9keV). It is much simpler to approximate the SED with a negative exponential distribution which has a relative SD of unity. As figure 1 shows, this results in a PH spectrum for 5.9keV x-rays with a FWHM of 16.2%. Since the effect of the PH spread makes only a minor contribution to the spatial resolution, this approximation is regarded as acceptable. (It is noted in figure 1 that the characteristic argon PH spectrum with the fluorescent escape peak at 3keV is reproduced.) The pulse heights of figure 1 are multiplied by the mean gas gain before further processing.

3.5 Electronic noise: In the model the electronic noise is added into the signal as a normal distribution (after gas amplification), quantified in terms of the number of root mean square (RMS) electrons contributed by the amplifier on each strip/bin. This is an exact representation of the situation in the case of a spatially digitised detector such as the GMSD. In the case of other forms of readout (e.g. delay line) the numbers are of purely relative significance since the gas gain is much higher than in the GMSD case but there are accompanying signal attenuations. To minimise computing, the noise is only added into bins containing electrons. This has no effect on the evaluated position because any practical electronic threshold must be set well above the noise level.

For the purposes of the present study, the details of a particular form of readout are not simulated since the purpose is to evaluate the best spatial resolution available independent of the readout mode. For this purpose very small spatial bins are chosen (5μm for argon and 2μm for xenon) and the

centroid of the hit pattern on the bins is evaluated for each event and that centroid value added to the spatial distribution of the ensemble of events (typically 50 000). The spatial resolution is then evaluated from this spatial spectrum (at a given x-ray energy) by measuring its FWHM in bins and multiplying by the bin width.

The code which implements the model has two main blocks – the set-up and the core functions. (The language used is PowerBasic.) The set-up block, apart from providing the essential housekeeping functions (dimensioning arrays and opening output files) defines all the essential parameters for the gas under study (shell binding energies, fluorescent yields, auger energies, diffusion constant, Fano factor, etc.). The detector/readout parameters are also defined (e.g. conversion depth, electronic noise) as is the range of x-ray energy to be explored and the energy step. The number of events in a position spectrum is also defined (N_x).

The core block implements the basic model in a sequence of three nested loops. The outer (x-ray energy) loop defines the x-ray energy at which a position spectrum is to be generated. At this stage the probabilities of interactions on each of the accessible atomic shells are evaluated along with the energy and mean range of the photo-electron (and the number of associated secondaries). The second (event) loop (performed N_x times at each energy) inserts all the variations which can occur for any event (e.g. interaction with which shell, with or without fluorescent conversion, adding the variability in the range of the primary). The final part of the code in this loop generates random directions in space (3-dimensions) for every primary electron range vector and projects it onto the readout axis (conventionally the readout direction has its segmentation along the x-axis). The interaction depth is assigned randomly in the z (drift) dimension over the specified conversion depth. (If the beam is incident in the z direction this is easily changed to a negative exponential distribution with the specification of an appropriate absorption length.) The third (secondary electron) loop follows the fate of the secondary electrons generated uniformly along the range vectors of the various primary electrons generated, dispersing them (in a normal distribution – $\sigma = \sigma_0\sqrt{z}$) down onto the x-axis according to the diffusion appropriate to their point of origin along the z-axis. Each electron is subjected to the gas amplification process as described above and the electronic noise superimposed. The dispersed secondaries are histogrammed into an array which represents the footprint of that event on the x-axis. For each electron this loop is performed E_e/W times for each primary electron and the variance of the Fano factor is randomly superimposed. When all the secondaries of all the primary electrons have been accumulated in the array of x-bins the centroid of the distribution is calculated (relative to the incident x-coordinate of the slit beam) and this value is histogrammed in the position spectrum array for the given x-ray energy. Finally, returning to the outer energy loop, the FWHM of the whole population (N_x) is evaluated and E_x and its accompanying FWHM printed to a disc file. This provides the basic output as a plot of FWHM as a function of the incident x-ray energy. However, provision is made to output the position spectrum of any chosen x-ray energy or any chosen event.

4. The Simulations

In order to eliminate detector structure effects the x-axis sampling bin width has been kept low compared with any possible spatial resolution obtainable; viz, 5μm for argon and 2μm for xenon. For each event the centroid of the footprint is evaluated. Since the position spectra are not normal in form, evaluation of the FWHM of the x-ray position spectrum from a simple statistic such as the root mean square error (σ_x) is not in general appropriate (as the position spectrum simulated for 5.9keV x-rays in argon (figure 2) shows). While the central core is a normal distribution, there are wider tails produced by the PEs from the L shell interactions. Thus the algorithm used is to find the maximum of the distribution and simply evaluate the width in bins at half the maximum of the peak. A logarithmic vertical axis is used to better show the low level tails.

Since a wide range of experimental parameters is possible, somewhat arbitrary standard conditions must be assumed for systematic comparisons to be made with the model. In practice, a gas gain of 1000 with an electronic noise of 1000 electrons RMS per bin was chosen (since this roughly corresponds with a well-found GMSD) and a $\sigma_0 = 0.2\text{mm}/\sqrt{\text{cm}}$, which corresponds to a generally achievable value with an argon/xenon mixture with a typical quencher at the optimal drift field. The active depth is set at 10mm. In terms of a 5.9keV x-ray the gain and noise figures chosen represent a signal to noise ratio (SNR) of ≈218. For other readout modalities (e.g. artificial delay lines on a wire counter), the gas gain is much higher but there are significant signal losses and increased amplifier noise, so that the figures chosen seem to represent a reasonable optimum for most forms of readout (i.e. in terms of SNR).

4.1 Comparison with experimental data: Systematic experimental measurements of the spatial resolution of imaging gas counters are rare and the precise conditions of different measurements vary enormously. The data of reference [15] present a consistent set in both argon and xenon mixtures, the only slight variation is that different conversion depths appear to have been used for different x-ray energies. The electronic noise contribution to the position resolution is estimated at 20μm. Figure 3 presents a comparison of the measurements of reference [15] with the predictions of the model under the standard conditions chosen. Given the impossibility of matching all the details of the experimental detector, the level of agreement seems quite satisfactory and generates confidence that when applied to a practical detector design it will give a realistic estimate of the spatial resolution obtainable.

It is worth noting (as pointed out in reference [15]) that over most of the range (1keV to 20keV) the spatial resolution is dominated by the PE range. The K shell edge in argon and the L shell edge in xenon extract energy from the PE so that characteristic improvements in the FWHM are seen just above the edges giving an optimum around 6keV for argon and 8keV for xenon. The consistently better resolution in xenon compared to argon is essentially due to shorter primary electron ranges in xenon caused both by its greater density and greater multiple scattering.

4.2 Physical modelling: The discussion of section 2 above indicates that the

different physical effects contributing to the spatial resolution should show a fairly simple parametric dependence on the x-ray energy (E_x). These effects may be summed up by the quadrature summation:

$$FWHM = \sqrt{\frac{a^2}{E_x} + \frac{b^2}{E_x^2} + \left(c\left(E_x - E_E\right)^d\right)^2} \qquad (1)$$

where the first term models the centroiding of the diffusion, the second takes account of the electronic SNR and the third the dispersion due to the PE range. E_E is the dominant absorption threshold energy of the gas atoms and the other constants depend variously on the diffusion and the readout details. In the last term, c and d are the constants determining the simplest parameterisation of the electron range in the gas.

Figure 4 shows that for the important part of the x-ray energy range (i.e. above the dominant absorption edges), excellent fits with equation (1) are possible, and it is interesting to note that the exponent of the electron range power law in argon (d) is 1.78, very close to the value obtained from the data in reference [15]. A similar fit is possible to the argon data below the K edge, probably because the electron range is clearly dominant; however, in the case of xenon the terms seem to be all comparable and no meaningful fit is possible.

4.3 Line Response Functions: In the practical experimental situation, the performance of a detector is generally characterised in terms of the line response function (LRF) i.e. to a slit beam of x-rays. The Monte-Carlo model permits the generation of the LRF for any desired x-ray energy (E_x). Figure 5 displays a sequence of LRFs for argon in the range E_x = 1keV to 20keV. Again they are displayed with a logarithmic vertical axis to accommodate the wide range of amplitudes. Up to $E_x \approx$6keV (figure 2) the core LRF remains a normal distribution but as the PE range comes to dominate the response (E_x>8keV) the LRF tends more and more to a "top hat" distribution. (N.B. the log scale in figure 5 tends to exaggerate this somewhat.) This agrees with the very rectangular LRF seen in ethane at 8keV in figure 5 of reference [15]. Clearly, useful spatial resolution in argon at 1 bar is limited to x-ray energies below 10keV. The departure of the LRF from a normal distribution means that different statistics used to evaluate the spatial resolution will deliver slightly different results – hence the decision to use the explicit FWHM rather than 2.36 times the second moment about the mean (σ) of the distribution.

Figure 6 shows the corresponding plot obtained from the model for xenon gas under the standard conditions. As with argon, the LRF grows dramatically above the optimum resolution energy as the PE range comes to dominate. However, the core LRF still remains a normal distribution (even at E_x=20keV), as figure 7 shows. This preserves more high (spatial) frequency information in the LRF compared with the corresponding argon LRF and so makes for a more useful detector at energies above 10keV. The 8keV peak in figure 7 can be compared with the experimental results presented in figure 6 of reference [15] where the low shoulders can be observed. The most obvious difference is the absence in the model of the wide spread very low level of

double hits caused by conversion of the L fluorescent x-ray in the detector volume. The Monte-Carlo model ignores these events. The M shell tail distribution in the 8keV LRF in figure 7 fits perfectly to a normal distribution with a FWHM of 141.6μm compared with the core FWHM of 45.1μm. Clearly (figure 6) this symmetry breaks down at energies above ≈16keV.

4.4 Systematic variation of operation parameters: All counter designs are compromises between experimental desiderata and the realities of physics and engineering limitations. While equation (1) gives a rough parametric guide to some of the inevitable trade-offs, the model permits explicit investigation of the effects on the spatial resolution of some of the more commonly varied parameters (conversion depth (d), diffusion constant (σ_0) and amplifier electronic noise (N_A)). Since it is the SNR (as discussed above) which determines the effect of the amplifier noise, the gas gain is held constant. (The avalanche induced excess noise factor in a gas avalanche process is found to remain essentially constant over a wide range of gas gain until the pulses are sufficiently large for UV feedback to introduce instability.) The parameters not being varied in a given set are held at the standard values (d=1cm, σ_0=0.2mm/√cm and N_A=1000 electrons (RMS).)

4.4.1 Spatial resolution as a function of conversion depth: Figure 8 shows the FWHM of the LRF as d is varied in argon from 5mm to 80mm (a likely range of practical detector drift distances). With the standard conditions, the conversion depth only has a significant effect on the FWHM for x-ray energies less than 3keV. In the typical region of argon application (around 6keV) the maximum variation is from 124μm to 148μm. Above this energy the electron range dominates totally over any diffusion effects.

In xenon (figure 9) the diffusion spreading plays a significant role in determining the FWHM up to ≈8keV above which the PE range begins to assert control. In this case the FWHM rises from ≈40μm to ≈90μm over the range of 5mm <= d <= 80mm with an almost uniform behaviour from E_x = 1keV up to 8keV.

4.4.2 Spatial resolution as a function of the diffusion constant: As noted in section 2.3 above, the SD of the (normal) diffusion footprint on the detection plane is $\sigma=\sigma_0\sqrt{z}$ where z is the drift distance of the electron cloud. Thus the effect of varying σ_0 on the low energy spatial resolution is expected to be significant. Figure 10 shows the simulation for argon with a range of σ_0 which could be plausibly encountered in a planar drift geometry with the usual (10% - 20%) of a typical quencher at drift fields of a few kV/cm at ambient pressure (0.1mm/√cm <= σ_0 <= 0.8). While at the lowest x-ray energies, the degradation of the FWHM over the range of σ_0 is almost linear (≈5:1), at the more practical energy of 6keV the effect is much reduced by the dominance of the PE range (i.e. the FWHM only increases from 125μm to 180μm). At higher energies the effect is negligible.

In xenon, the much lower PE range means that the significant effect of σ_0 on the FWHM is prolonged to much higher energies (≈10keV). Figure 11 shows a fairly uniform increase of ≈4:1 of the FWHM over the energy range 1keV to 8keV with the PE range effect not dominating until an energy of ≈15keV is reached. The implication of this graph is that, while the stochastic noise is still playing a significant role for E_x <10keV, it is clearly important to get the drift conditions optimised in a xenon-filled detector (i.e. σ_0 minimised) if the good spatial resolution promised by the low PE range is to be used to good advantage.

4.4.3 Spatial resolution as a function of amplifier electronic noise: The specific RMS noise values (N_A) used in the simulation refer to the particular case of a strip readout GMSD. However, as noted above, with the standard avalanche gain chosen to be 1000, these noise values correspond roughly to an SNR of 200 for a 6keV x-ray energy (a standard value for testing gas counters). The noise values are chosen to ascend in binary steps so that the SNR is decreasing correspondingly from 200 to 12.5 in the simulations.

As formula (1) predicts, a situation of zero electronic noise simply results in a FWHM determined by the various physical factors inherent in the gas counter and (in fact) the electronic noise makes no significant contribution (except below E_x = 2keV) until N_A reaches 4000 electrons (SNR ≈ 50 at 6keV) in argon. The FWHM in argon (figure 12) is so dominated by the PE range that even with the very poor noise figure of 16 000 electrons, it is only increased by ≈2:1 relative to the zero noise case. A curious feature of figure 12 is that great electronic noise appears to improve the FWHM in the high energy region which is normally dominated by the PE range effect. Since this feature also applies to the xenon data it will be discussed below.

As figure 13 shows, the FWHM of the LRF in xenon is much more sensitive to the electronic noise than that of argon (because the PE range contribution is so much smaller). While one is allowed about 2000 electrons of noise before the FWHM is degraded, it deteriorates rapidly with higher noise and the effect continues to very high x-ray energies (>15keV). However, as in argon, an anomalous improvement is seen at the very limit of the energy range (20keV).

Figures 14 and 15 compare the position spectra (LRF) for 20keV x-rays with 1000 electrons and 16 000 electrons RMS noise in argon and xenon respectively. In argon (figure 14) the low noise peak shows the characteristic top-hat distribution noted experimentally in reference [15] when the PE range is dominant. A large electronic noise signal of 16 000 electrons (being intrinsically a normal distribution) produces a much sharper peak, which (nevertheless) is clearly wider than the top-hat. When the standard deviations of the two distributions are calculated the 1000 electron distribution has FWHM = 2209μm and the

16 000 electron curve has FWHM = 256.7μm, (evaluated as 2.36σ) reversing the order seen in the FWHM values calculated by the model. The important aspect of the situation is that the high noise LRF has high frequency components lacking in the low noise (top-hat) LRF and will consequently yield better imaging. This explains the decision to use the literal FWHM statistic in the program rather than the expression 2.36σ which only applies to normal distributions which are not valid at the higher x-ray energies. In other words the improved high energy LRF with large electronic noise seen in figures 12 and 13 are good guides to the imaging capability of the detectors.

The same reversal of the LRF resolution is seen in the xenon data (figure 15) although the PE range has not become dominant enough to distort the LRF from a quasi-normal distribution. The statistical figures are FWHM = 54.8μm for the 1000 electron curve and 64.9μm for the 16 000 electron curve at E_x=20keV.

4.5 Simulations of hyperbaric operation: Hyperbaric operation of gas-filled x-ray detectors is usually undertaken to enhance the detection efficiency of the devices as it falls off rapidly (even with xenon) above $E_x \approx 10$keV. However, the Monte-Carlo model shows (in agreement with the experimental results of reference [16]) that hyperbaric gas pressures improve the spatial resolution by suppressing the effect that the primary electron ranges have on the LRF. Since charged particle ranges scale inversely with the gas density, and therefore with the pressure, it is simple to modify the model to explore the effect of raising the gas pressure on the spatial resolution. Figure 16 shows the effect on the FWHM of the LRF of raising the gas pressure (P) from 1 bar to 5 bars in argon. (The pressures quoted are absolute values.) In the high energy region where the PE range dominates, the FWHM is approximately inversely proportional to P with the value at 20keV falling from 282.0μm to 58.4μm.

In the lower energy range even the small increase of P to 2bar leads to a substantial improvement with the FWHM remaining below 100μm up to $E_x \approx$ 7keV while at 5bar pressure it remains below this level up to ≈10keV. The optimum resolution (at 6keV) is ≈34μm and is on a rough par with the xenon resolution at ambient pressure. In figure 17 we see that even at 5bar pressure the LRF in argon at E_x = 11keV is still slightly "top-hat" in shape rather than truly normal.

The results of varying P in a xenon-filled device (figure 18) are similar in principle to those for argon with the difference that the FWHM is consistently lower. Again, as in argon, a simple doubling of P makes a very useful improvement with an optimum of FWHM = 30μm at E_x = 8keV. At P = 5 bar the optimum resolution is 24μm at $E_x \approx$ 8keV and the FWHM stays below 30μm up to $E_x \approx$ 12keV. In the high energy region, the FWHM stays below 100μm up to 20keV and as figure 19 shows, the LRF remains substantially a normal distribution.

In the hyperbaric studies the standard conditions (gain, noise, diffusion) have been adhered to for consistency. However, it is worth noting that some changes are liable to occur with hyperbaric operation. Since the maximum stable gain tends to reduce as P is increased the electronic SNR will deteriorate somewhat. On the compensating side, the review of diffusion data given in reference [13] indicates that if a good fraction of quencher is retained and higher drift fields are tolerable, then a considerable improvement in σ_0 can be expected (possibly down to $\approx 0.1 mm/\sqrt{cm}$). Thus the low energy data presented in figures 16 and 18 are likely to be realistically attainable.

5. Conclusion

The Monte-Carlo model developed primarily as a design tool for x-ray imaging gas microstrip counters has proved to be a powerful tool for exploring the limits set by purely physical processes on the spatial resolution obtainable in gas avalanche counters. All the significant physical "spread" factors have been included explicitly, omitting only the actual spread of the single electron avalanche. The simulations of reference [17] show that the extent of the avalanche along a typical wire of 25μm diameter is about two wire diameters (i.e. ≈50μm). Since this is almost an order of magnitude smaller than the diffusion spread over a typical drift distance, this effect is not expected to have a significant effect on the LRF. (In gas mixtures in which UV-initiated gain comes into play the avalanche dimensions would generate avalanches of significant dimensions e.g. hundreds of microns.)

The standard parameters chosen for the purposes of theoretical comparisons can all be changed at will to simulate the conditions in any proposed experimental device. In particular, the sampling bin widths can be increased to correspond to the realistic sampling widths of actual detectors and the resulting "sampling noise" included.

The findings of the modelling work have all been spelled out above and it need only be noted that (not only in respect of detection efficiency but also in respect of the achievable spatial resolution) xenon-based gas mixtures perform considerably better than those based on argon. This advantage persists over the whole energy range studied ($1keV < E_x < 20keV$) though it is particularly great at the high energy end. The model has also shown that considerable advantages can accrue from the use of (quite mild) hyperbaric operation, in the matter of spatial resolution as much as in the matter of detection efficiency.

References

1. A. Oed, Nucl. Instr. and Meth. A 261 (1988) 351.

2. F. Sauli, Development of gas microstrip chambers for radiation detection and tracking at high rates, CERN/DRDC/94-45 (1995)

3. J.E. Bateman, J.F. Connolly, G.E. Derbyshire, D.M. Duxbury, J. Lipp, R.C. Farrow, W.I. Helsby, R. Mutikainen, I Suni, Nucl. Instr. and Meth. A 477 (2002) 340-346.

4. J.E. Bateman, N.J. Rhodes, R. Stephenson, A 477 (2002) 365-371.

5. J.E. Bateman, N.J. Rhodes, R. Stephenson, Rutherford Appleton Laboratory Report, RAL-TR-98-024.

6. R. Berliner, D.F.R. Mildner, O.A. Pringle, J.S. King, Nucl. Instr. and Meth. 185 (1981) 481.

7. S.N. Kaplan, L. Kaufman, V. Perez-Mendez, K. Valentine, Nucl. Instr. and Meth. 106 (1976) 397.

8. R. Allemand and G. Thomas, Nucl. Instr. and Meth. 137 (1976) 141.

9. R.A. Lewis, W.I. Helsby, A.O. Jones, C.J. Hall, B. Parker, J. Sheldon, P. Clifford, M. Hillen, I. Sumner, N.S. Fore, R.W.M. Jones, K.M. Roberts, Nucl. Instr. and Meth. A 392 (1997) 32-41.

10. J.E. Bateman, G.E. Derbyshire, D.M. Duxbury, A.S. Marsh, N.J. Rhodes, E.M. Schooneveld, E.J. Spill, R. Stephenson, Rutherford Appleton Laboratory Report RAL-TR-2004-027.

11. J.E. Bateman, Nucl. Instr. and Meth. B 184 (2001) 478-489.

12. G.F. Knoll, Radiation Detection and Measurement, John Wiley and Sons, New York, 1989 (Chapter 6).

13. A. Peisert and F. Sauli, Drift and diffusion of electrons in gases: a compilation, CERN 84-08, 1984.

14. W.H. McMaster, N. Kerr Del Grande, J.H. Mallett, J.H. Hubbell, University of California, Livermore, UCRL-50174, Sec. II.

15. G.C. Smith, J. Fischer, V. Radeka, IEEE Trans. Nucl. Sci. NS-31, No. 1, 1984, 111-115.

16. J. Fischer, V. Radeka, G.C. Smith, Nucl. Instr. and Meth. A 252 (1986) 239-245.

17. M. Matoba, T. Hirose, T. Sakae, H. Kametami, H. Ijiri, T. Shintake, IEEE Trans. Nucl. Sci. NS-32, No. 1, 1985, 541-544.

Figure Captions

1. The simulated pulse height spectrum given by the model for the detection of 5.9keV x-rays in argon. The spectrum is measured in terms of the number of secondary electrons per event before they are shared among the detector bins – hence the lack of tails usually seen in a practical detector.

2. The simulated position spectrum for a slit beam of 5.9keV x-rays in argon.

3. A comparison of the spatial resolution obtainable from argon and xenon detectors as a function of the x-ray energy (1keV – 20keV) as determined by the measurements of Smith et.al. [15] and the Monte-Carlo Model (with the standard conditions).

4. A plot of the simulated spatial resolution data of figure 3 fitted with parameterisations of the form of equation (1).

5. Modelline response functions (LRF) in argon as a function of x-ray energy.

6. Modelline response functions (LRF) in xenon as a function of x-ray energy.

7. Model LRFs in xenon at E_x=8keV and 20keV with associated normal fits to the core distributions.

8. The FWHM of the model LRF in argon as a function of x-ray energy when the conversion depth is varied between 5mm and 80mm.

9. The FWHM of the model LRF in xenon as a function of x-ray energy when the conversion depth is varied between 5mm and 80mm.

10. The FWHM of the model LRF in argon as a function of x-ray energy when the diffusion constant σ_0 is varied between 0.1mm/$\sqrt{cm}$ and 0.8mm/$\sqrt{cm}$.

11. The FWHM of the model LRF in xenon as a function of x-ray energy when the diffusion constant σ_0 is varied between 0.1mm/$\sqrt{cm}$ and 0.8mm/$\sqrt{cm}$.

12. The FWHM of the model LRF in argon as a function of x-ray energy when the electronic amplifier noise is varied between 0 and 16 000 electrons RMS.

13. The FWHM of the model LRF in xenon as a function of x-ray energy when the electronic amplifier noise is varied between 0 and 16 000 electrons RMS.

14. Simulated LRFs for 20keV x-rays in an argon-filled detector with 1000 electrons electronic noise (squares) and 16 000 electrons (circles).

15. Simulated LRFs for 20keV x-rays in a xenon-filled detector with 1000 electrons electronic noise (squares) and 16 000 electrons (circles).

16. The simulated FWHM of the LRF in argon as a function of the x-ray energy at increasing (absolute) gas pressures.

17. The LRF of 11keV x-rays in an argon-filled counter at P = 5bar.

18. The simulated FWHM of the LRF in xenon as a function of the x-ray energy at increasing (absolute) gas pressures.

19. The LRF of 20keV x-rays in an xenon-filled counter at P = 5bar.

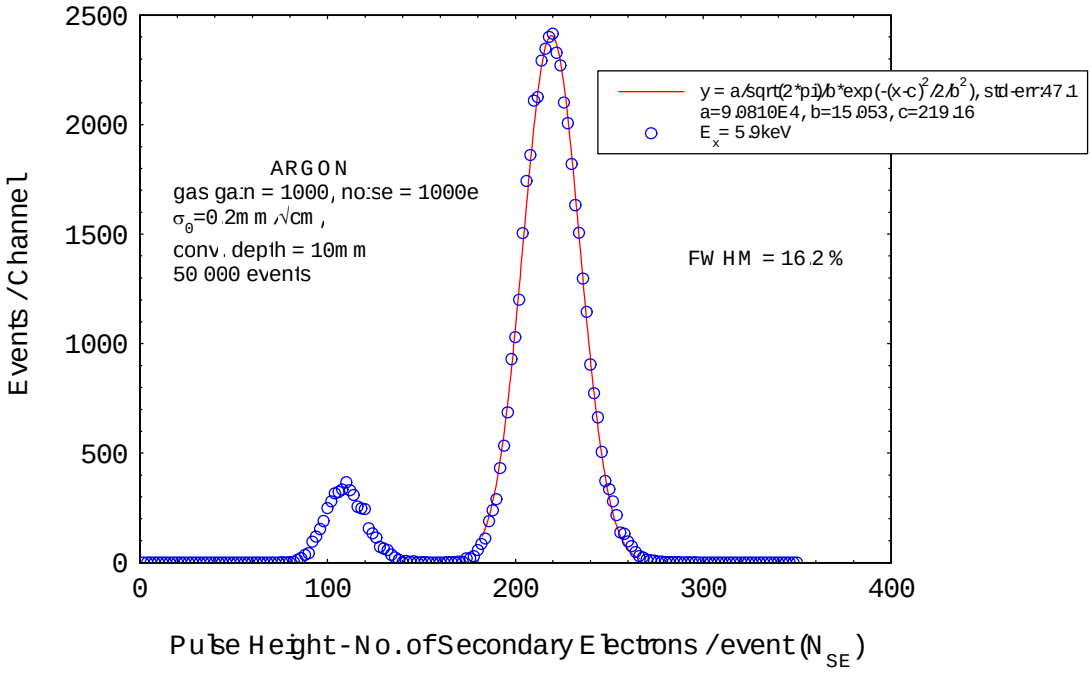

Figure 1

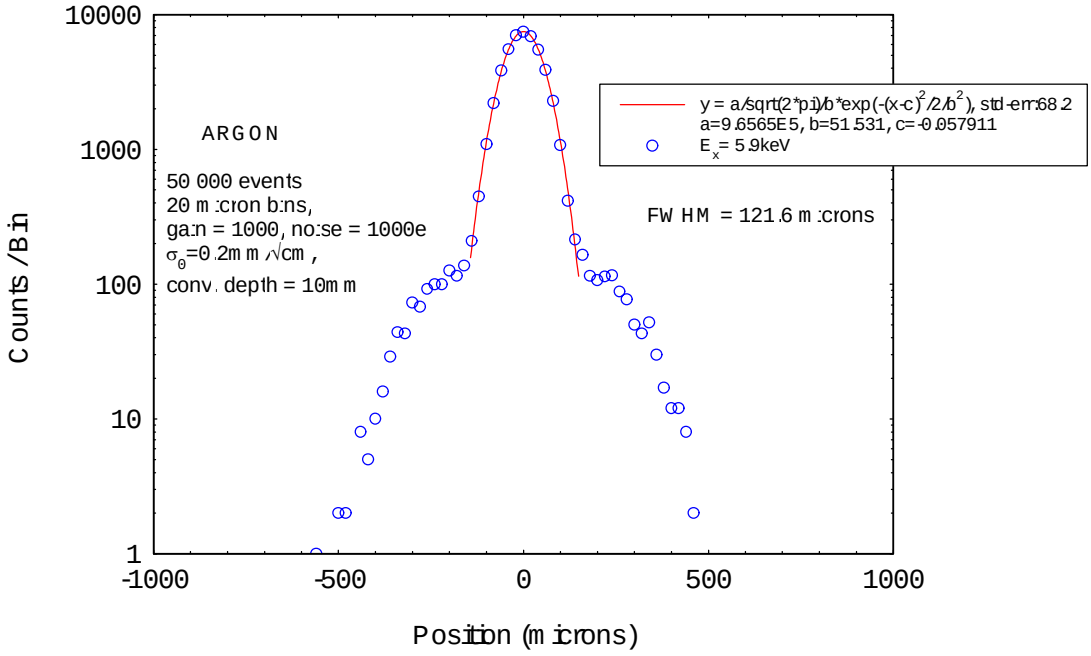

Figure 2

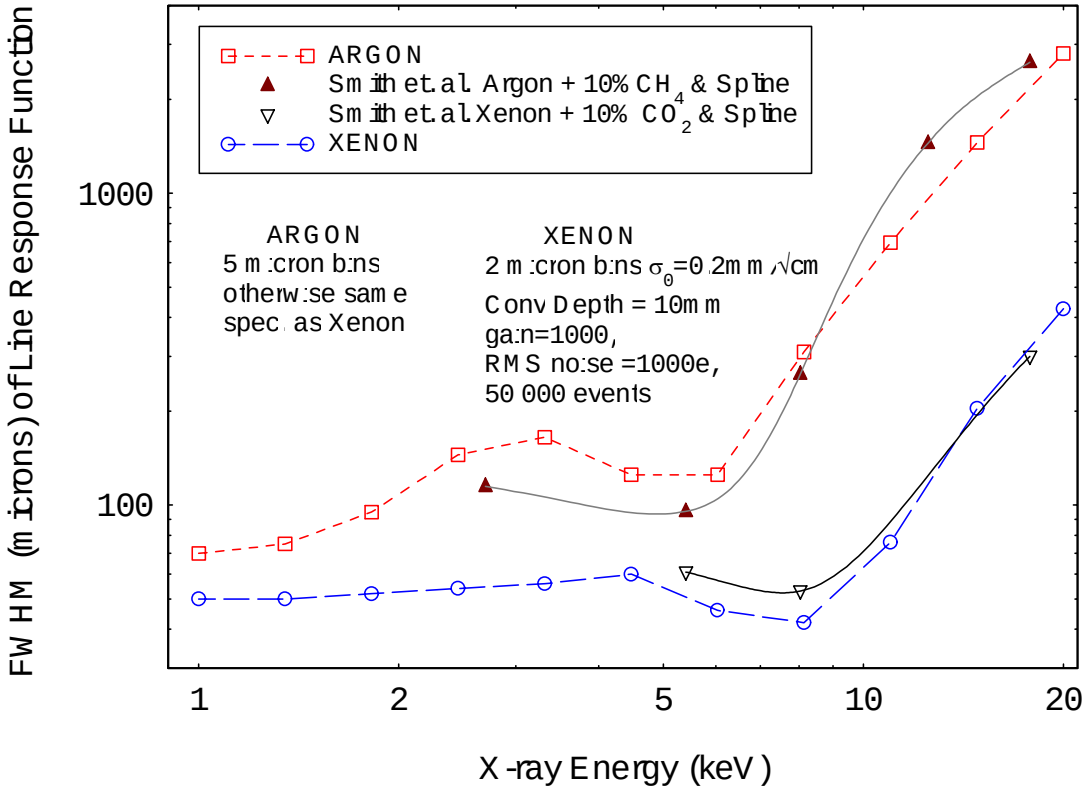

Figure 3

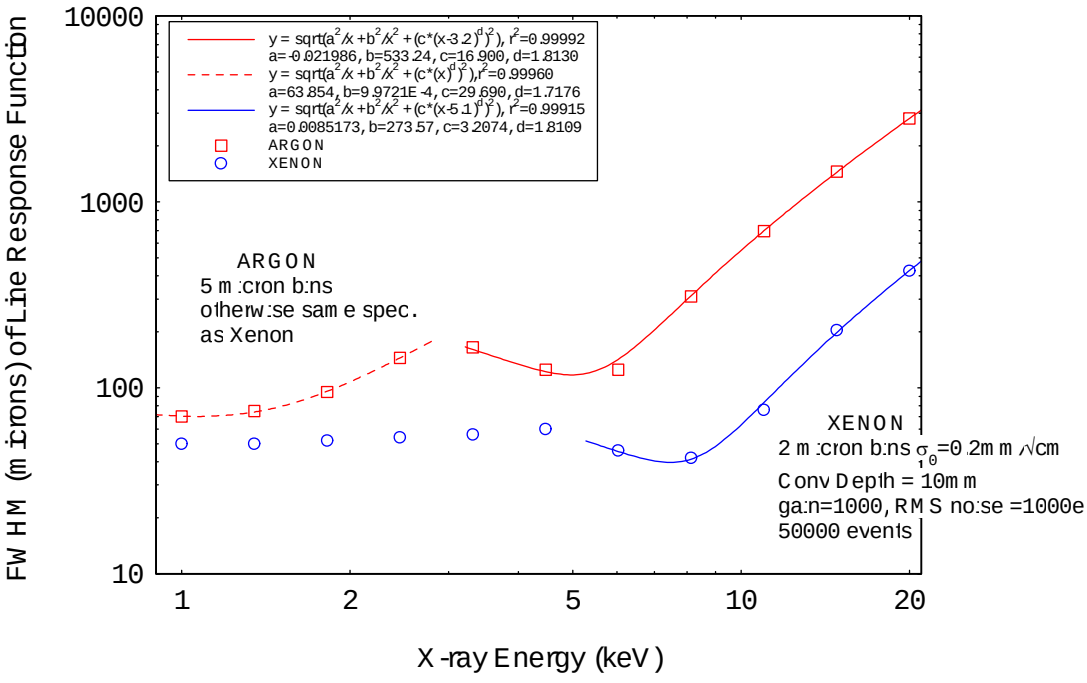

Figure 4

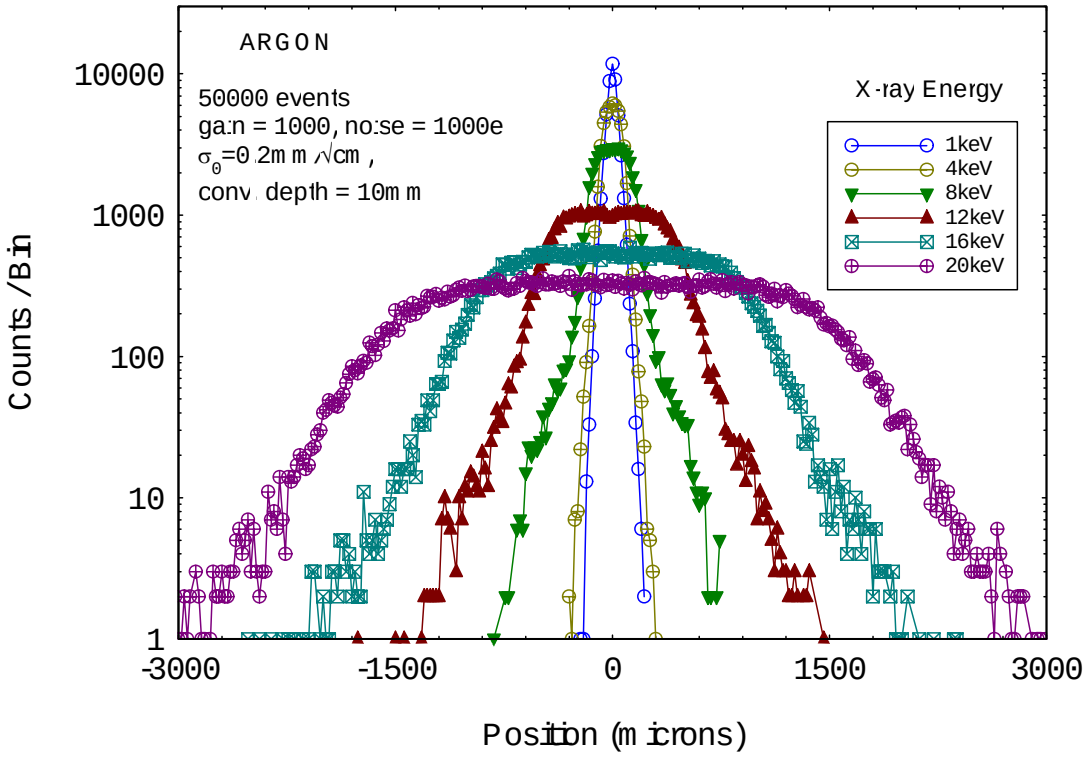

Figure 5

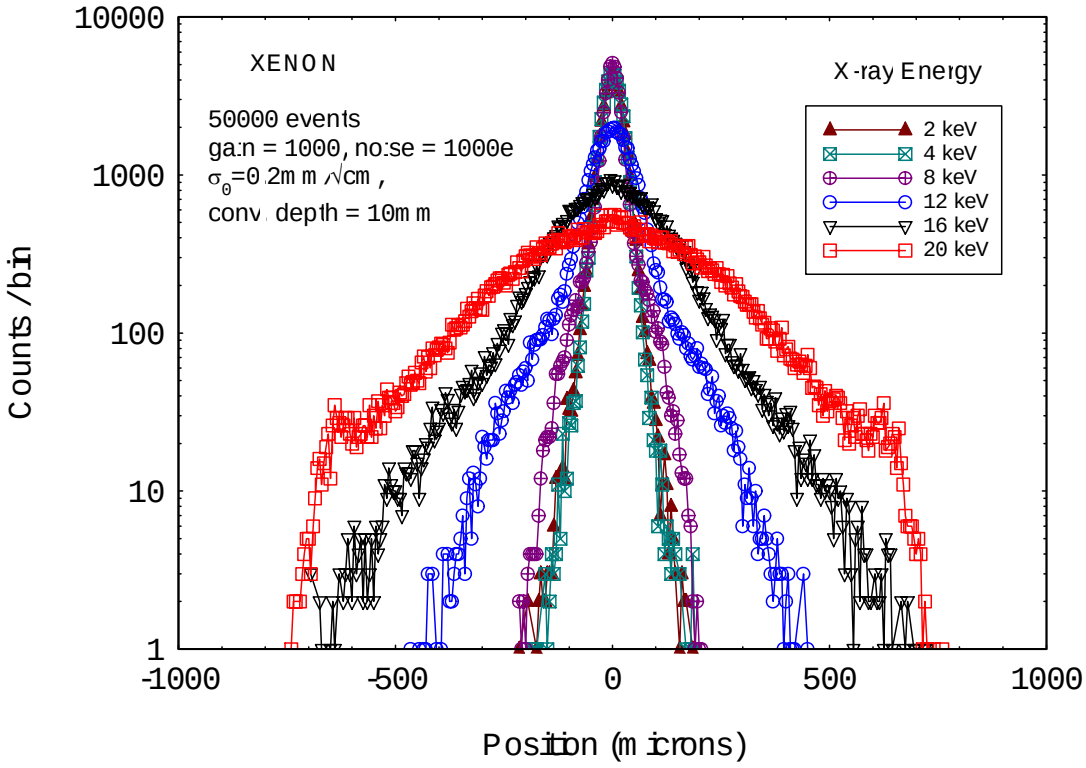

Figure 6

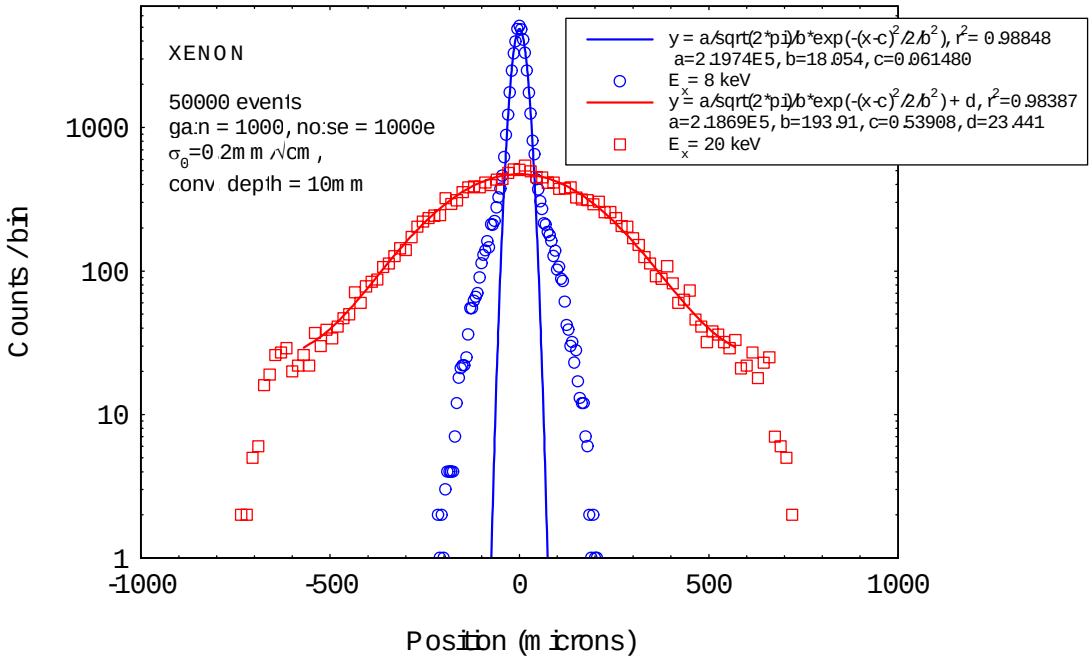
XENON
50000 events
gain = 1000, noise = 1000e
σ0=0.2mm/√cm,
conv. depth = 10mm
y = a/sqrt(2*pi)/b*exp(-(x-c)^2/2/b^2), r^2= 0.98848
a=2.1974E5, b=18.054, c=0.061480
Ex = 8 keV
y = a/sqrt(2*pi)/b*exp(-(x-c)^2/2/b^2)+d, r^2=0.98387
a=2.1869E5, b=193.91, c=0.53908, d=23.441
Ex = 20 keV
Counts/bin
1000
100
10
1
-1000
-500
0
500
1000
Position (microns)

Figure 7

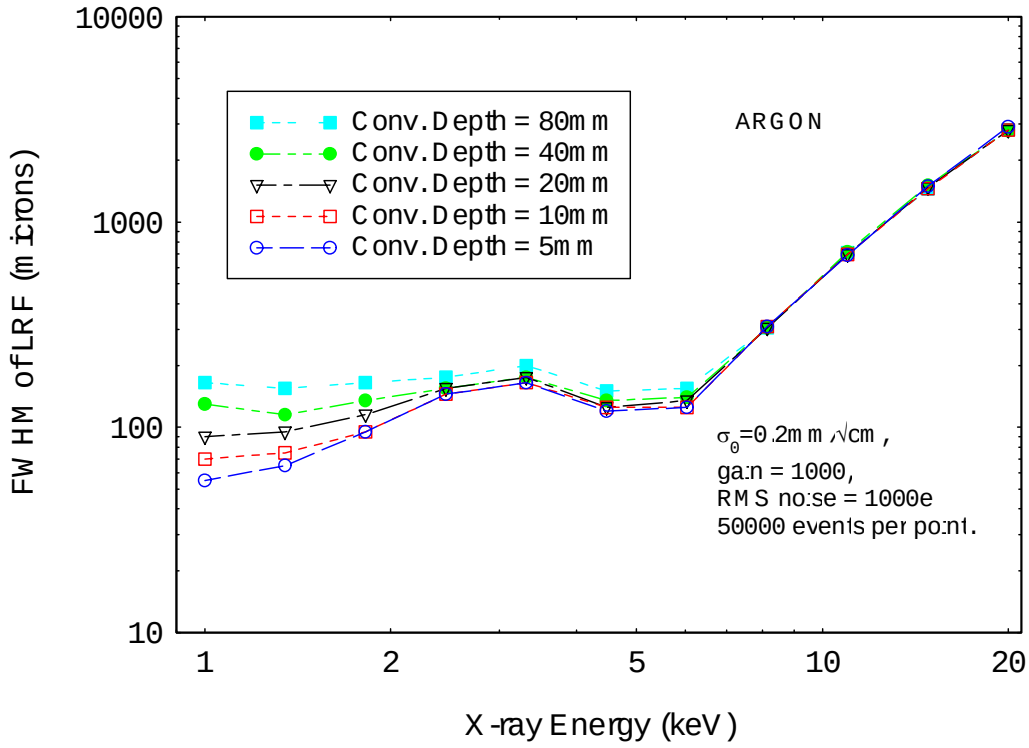

Figure 8

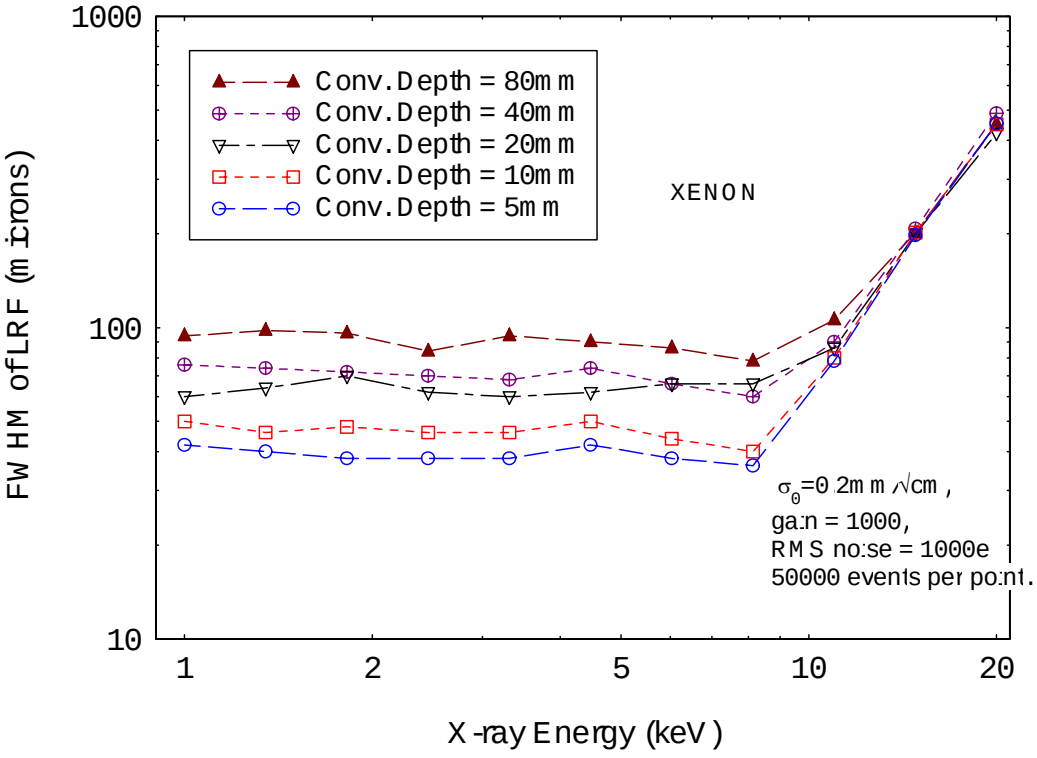

Figure 9

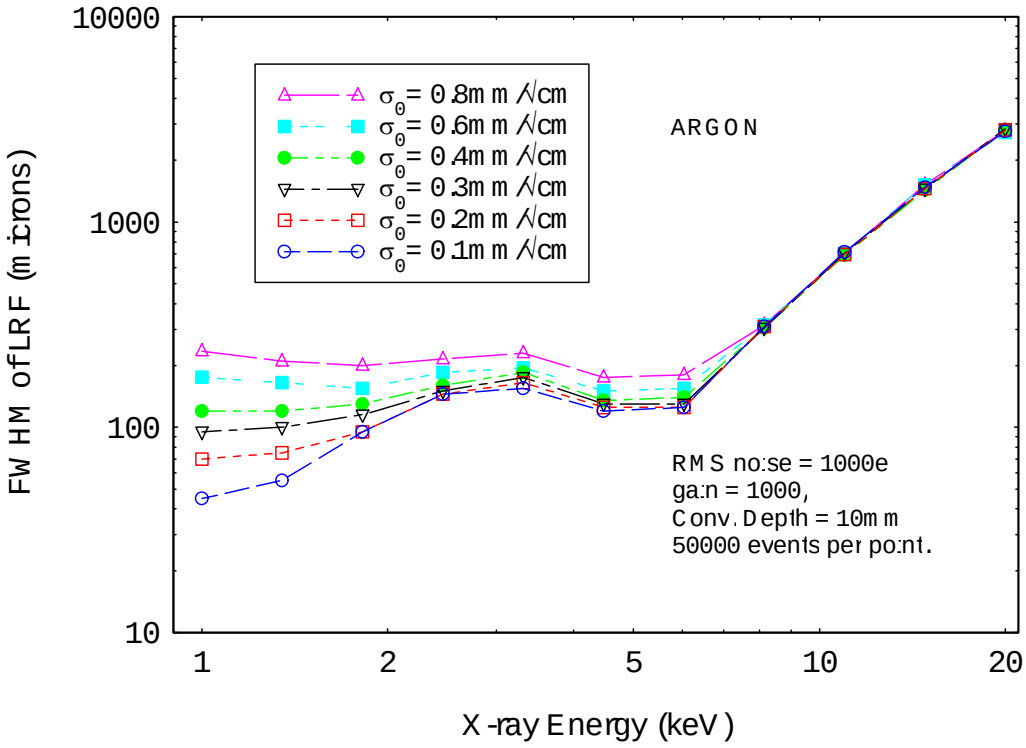

Figure 10

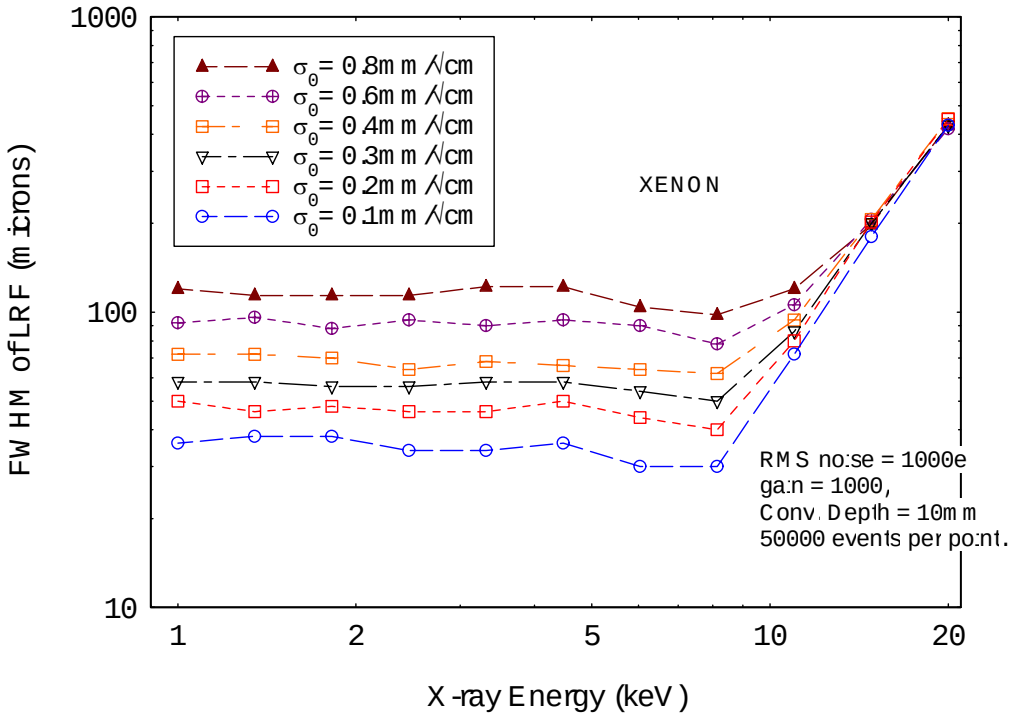

Figure 11

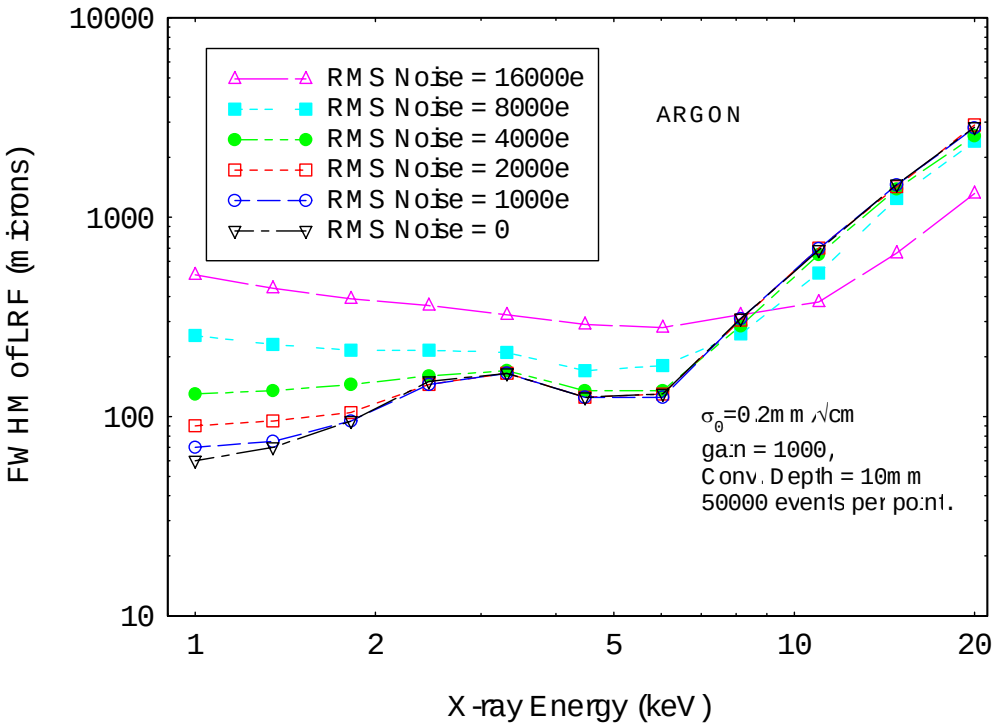

Figure 12

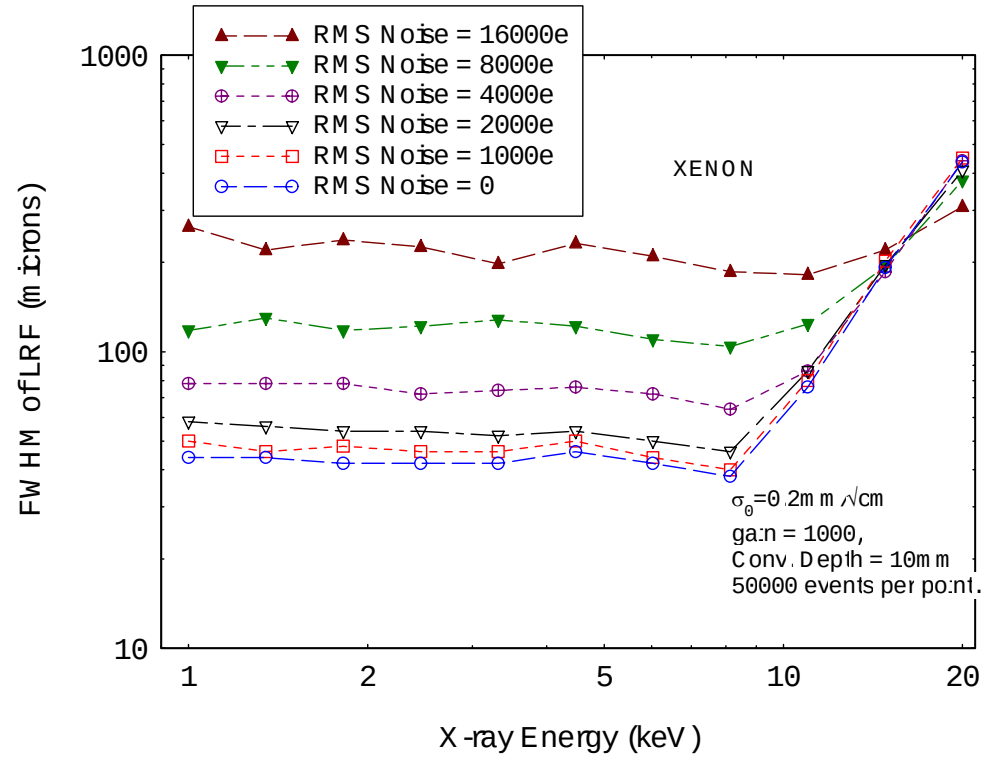

Figure 13

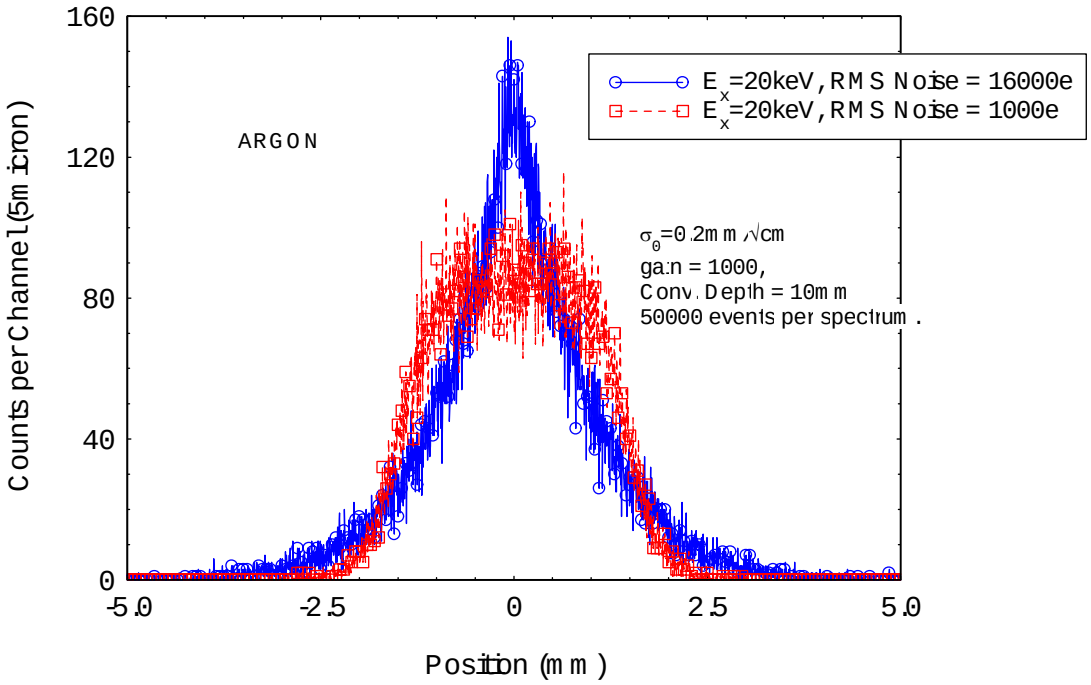

Figure 14

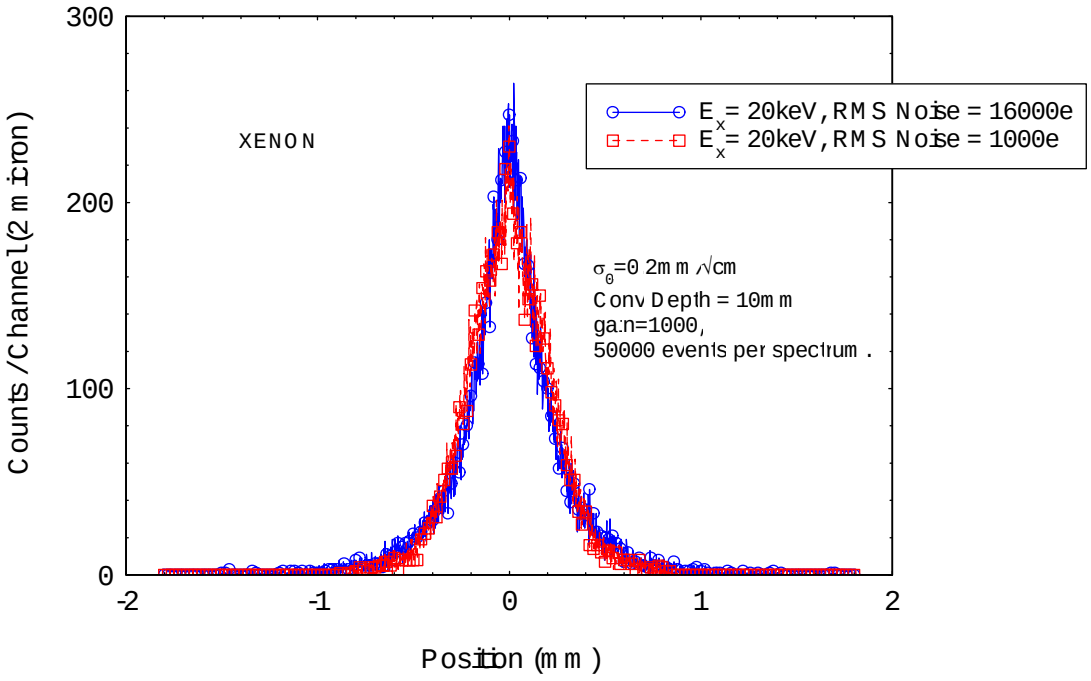

Figure 15

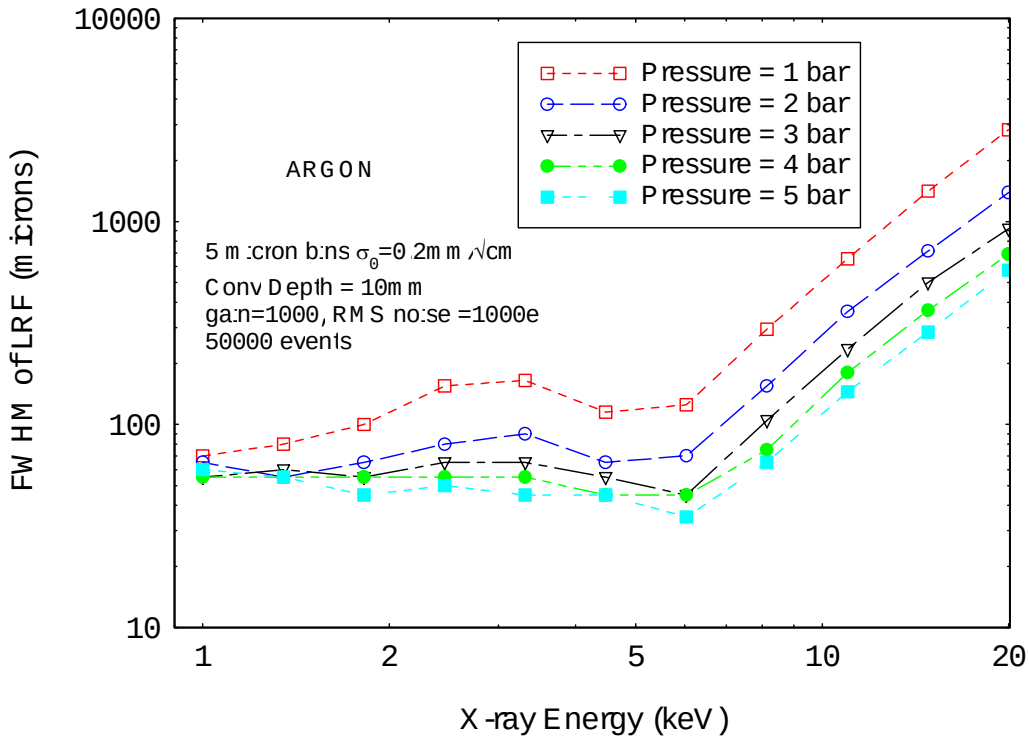

Figure 16

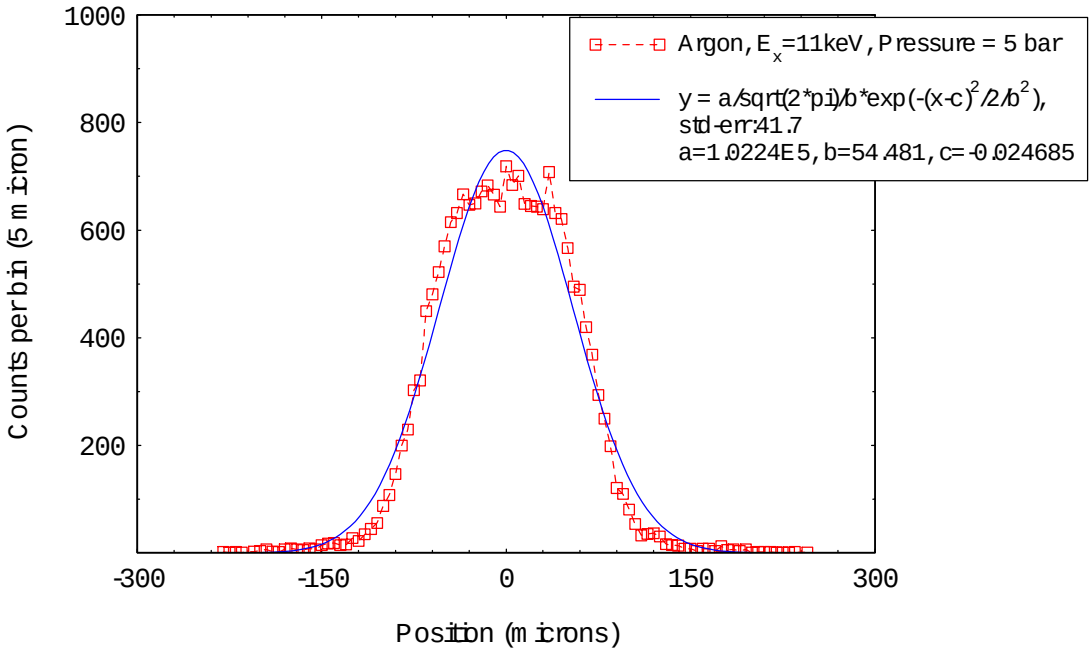

Figure 17

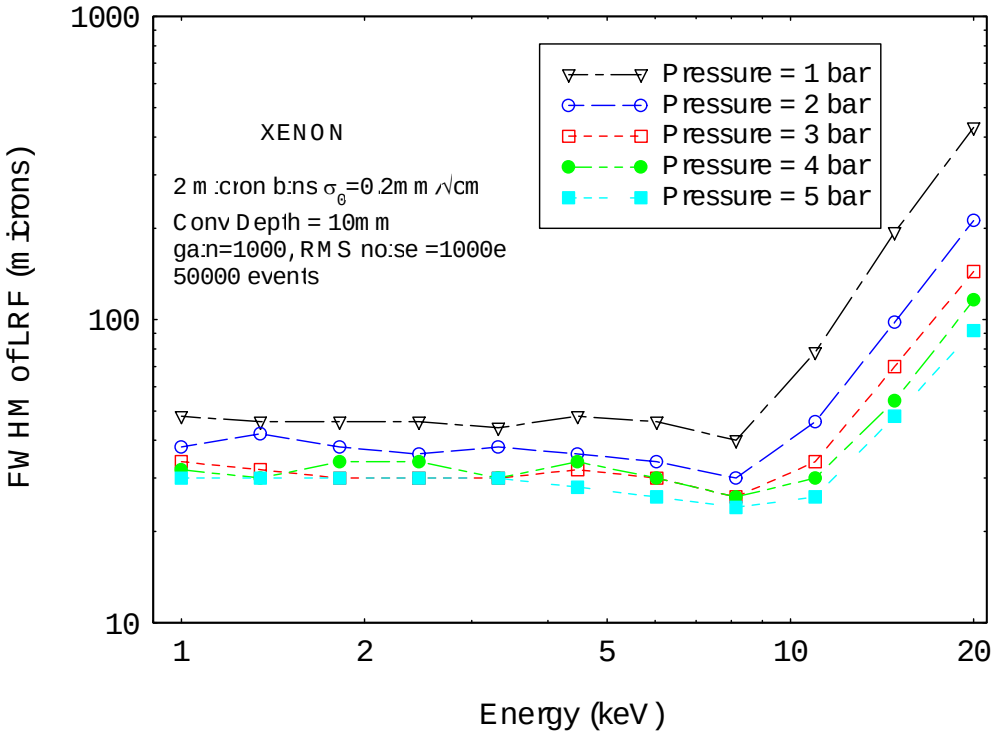

Figure 18

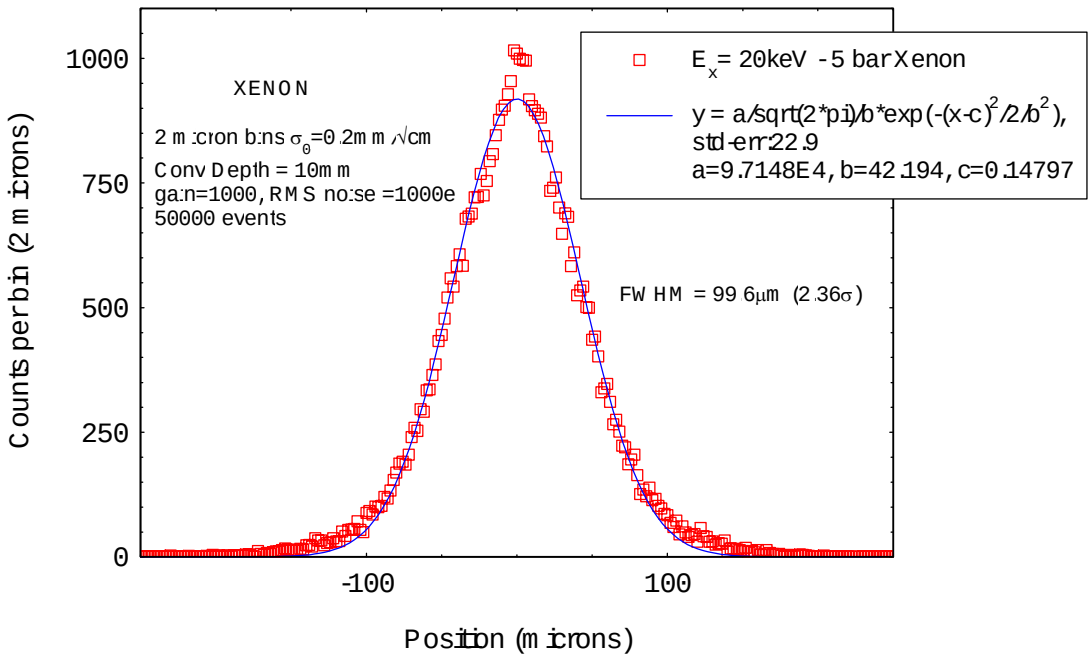

Figure 19